Taylor & Francis
Taylor & Francis Group

An integrated algorithm for estimating regional latent heat flux and daily evapotranspiration

Y. ZHANG*†‡, C. LIU†, Y. LEI†, Y. TANG‡, Q. YU§, Y. SHEN† and H. SUN†

†Shijiazhuang Institute of Agricultural Modernization, CAS, 286 Huaizhong Rd, Shijiazhuang, 050021, P.R. China

‡Environmental Biology Division, National Institute for Environmental Studies, Onogawa 16-2, Tsukuba 305-8506, Japan

§Luancheng Agro-ecosystem Station, Institute of Geographic Sciences and Natural Resources Research, Chinese Academy of Sciences, No Jia 11, Datun Road, Anwai, Beijing 100101, P.R. China

Using remote-sensing data and ground-based data, we constructed an integrated algorithm for estimating regional surface latent heat flux (LE) and daily evapotranspiration (ET_d). In the algorithm, we first used trapezoidal diagrams relating the surface temperature and fractional vegetation cover (f_c) to calculate the surface temperature–vegetation cover index, a land surface moisture index with a range from 0.0 to 1.0. We then revised a sine function to assess ET_d from LE estimated for the satellite's overpass time. The algorithm was applied to farmland in the North China Plain using Landsat Thematic Mapper (TM)/ Enhanced Thematic Mapper Plus (ETM$^+$) data and synchronous surface-observed data as inputs. The estimated LE and ET_d were tested against measured data from a Bowen Ratio Energy Balance (BREB) system and a large-scale weighing lysimeter, respectively. The algorithm estimated LE with a root mean square error (RMSE) of $50.1 \, \mathrm{W \, m^{-2}}$ as compared to measurements with the BREB System, and ET_d with an RMSE of $0.93 \, \mathrm{mm \, d^{-1}}$ as compared with the measurement by the lysimeter. Sensitivity analysis showed that changing meteorological variables have some influence on LE, while variation of f_c has little effect on LE. The test of the model in the study indicated that the improved algorithm provides an accurate and easy-to-handle approach for assessing regional surface LE and ET_d. Further improvement can be achieved in the assessments if we increase the accuracy of some key parameters on a large regional scale, such as the minimum stomatal conductance and the atmospheric vapour pressure deficit.

1. Introduction

Surface evapotranspiration plays an important role in the global water cycle. Depending on its magnitude, surface evapotranspiration can impact on climate at various spatial and temporal scales. Regional surface evapotranspiration is often used for the estimation of agricultural production, runoff prediction, recharge prediction, and land use planning (Kustas and Norman 1996). It is therefore essential to accurately estimate regional surface evapotranspiration (*ET* is usually in

*Corresponding author. Email: zhang.yongqiang@nies.go.jp; zhangyq@igsnrr.ac.cn

units of volume per unit area, while latent heat flux, *LE*, is given in units of energy) in order to explore climate dynamics and terrestrial ecosystem productivity (Churkina *et al.* 1999).

In most conventional techniques, point *ET* measurements are scaled up for regional *ET*. Such approaches are often largely limited by the dynamic nature and regional variation of *LE* (Li and Lyons 1999). During recent decades, remote sensing techniques have greatly improved. They provide us with more efficient tools for scaling up *LE* to larger spatial and longer temporal scales by using such parameters as radiometric surface temperature, albedo, and vegetation index (*VI*) in a globally consistent and economically feasible manner (Kustas and Norman 1996, Xue *et al.* 1998, 2000).

Evapotranspiration can be determined from the energy balance residual, which is itself estimated using net radiation (R_n), soil heat flux (G), and sensible heat flux (H) based on a combination of remote sensing and *in situ* observations. It is easy to obtain R_n from measurements, especially under clear-sky conditions. G is usually not considered to be a major source of uncertainty for the surface energy budget, although for instantaneous estimation this term could be as large as the sensible or latent heat flux (Jiang and Islam 2001). One of the most difficult issues is the estimation of H. The sensible heat flux here is a function of aerodynamic surface temperature (T_{aero}), which cannot be measured by sensors, but is usually replaced by land surface temperature (T_s), which could result in a 2–3°C error (Jiang and Islam 2001). Thus, significant uncertainty is present in the estimation of H with the classical aerodynamic formulation and T_s (Stewart *et al.* 1994). As a result, *LE* is estimated with an error greater than 50% (Stewart *et al.* 1994, Jiang and Islam 2003). In addition, air temperature (T_a), which is interpolated to a T_a regional map using observed values at meteorological sites, contributes a significant error to H. In order to reduce estimated errors of H, thermal inertial models are developed to calculate H directly (Cracknell and Xue 1996).

Another approach for the estimation of *ET* is the *VI*-T_s method. This approach is based on the observation that T_s decreases with an increase in the density of vegetation through latent heat transfer, although a decrease in surface temperature is modulated by the synoptic state of the atmosphere as well as by the aerodynamic and canopy resistance operating at the surface (Nemani and Running 1989). Changes in the slope of the normalized difference vegetation index (*NDVI*)-T_s scatterplot in a growing season have been found to track the modelled surface conductance in a semiarid ecosystem (Nemani and Running 1989). On continental scales, the slope of T_s/*NDVI* is strongly correlated with the crop-moisture index by an exponential function (Nemani *et al.* 1993). Based on a theoretical understanding of the crop water stress index (Jackson 1991), an algorithm has been developed to estimate the water deficit index through a simple geometric consideration of the trapezoidal diagram between *VI* and the difference between T_s and air temperature (T_a) (Moran *et al.* 1994, 1996). In the algorithm, the four vertices of a trapezoid are calculated from the *in situ* meteorological data according to the impact of surface soil moisture on the difference between T_s and T_a (Moran *et al.* 1994). On the other hand, an inversion method based on a soil vegetation atmosphere transfer (SVAT) model has been established to estimate soil water availability (M_0) from a triangular *NDVI*-T_s relationship (Carlson *et al.* 1995a, Gillies *et al.* 1997). The SVAT model, which provides a nonlinear solution for M_o and surface energy fluxes in the interior of the triangle (Gillies *et al.* 1997), has recently been used in many different studies.

The triangular $NDVI$-T_s relationship is used to estimate the vegetation temperature and air temperature for ET estimation (Boegh *et al.* 1999). A two-step linear interpolation scheme in the $NDVI$-T_s triangle is applied to obtain the Priestley–Taylor parameter value for each of the pixels in an image (Jiang and Islam 2001). The triangular $NDVI$-T_s diagram is also used to estimate maximum soil temperature, soil temperature, and air temperature in calculating the evaporative fraction (EF) of bare soil (Nishida *et al.* 2003). The VI-T_s triangle (or trapezoid) method has clear advantages of simplicity and consistency. It can obtain the surface soil moisture index with remotely sensed data, or with a combination of remotely sensed data and some surface meteorological data. The method, however, seems difficult for estimating the 'wet edge' of the triangle (or trapezoid) where surface ET is up to potential evapotranspiration (LE_p) because of interference from clouds, sloping terrain, and standing water (Moran *et al.* 1994). LE estimated with the $NDVI$-$(T_s$-$T_a)$ trapezoid method often tends to be out of the range between zero and LE_p (Moran *et al.* 1996).

Remotely sensed data provide regional instantaneous information, e.g. T_s. Thus, LE can be obtained at the satellite's overpass time. In many cases, ET_d may be a more interesting parameter than instantaneous LE. Several methods have thus been developed to estimate ET_d from instantaneous LE (Jackson *et al.* 1983, Nichols and Cuenca 1993). Jackson *et al.* (1977) estimated ET_d by integrating daily net radiation and the midday difference between surface temperature and air temperature with simple linear regressions. The method was improved later (Carlson *et al.* 1995b, Dunkel and Szenyán 2000, Lagouarde 1991, Sandholt and Andersen 1993). Assuming that the diurnal course of LE would generally follow the course of solar radiation throughout the daylight period, Jackson *et al.* (1983) first calculated ET_d with midday LE using a sine function. This approach is widely used for ET_d estimation not only at patch scales, but at regional scales (Boegh *et al.* 1999, Ibanez and Castellvi 2000, Lagouarde 1991, Zhang and Lemeur 1995, Zhang *et al.* 1995). However, our preliminary examination found that the method overestimates ET_d because it overestimates the solar radiation and LE at early morning and late afternoon. Nichols and Cuenca (1993) first used the midday evaporative fraction to predict ET_d and they also reported that this approach resulted in a consistent 25–40% over-prediction compared with mean measured daily values, even though a strong correlation exists between the midday and all-day mean evaporative fractions under clear skies.

To assess the regional surface energy fluxes and ET_d more precisely, we developed a new algorithm. In this approach, we first applied the T_s–f_c trapezoidal diagram to estimate the dry edges and the wet edges of the diagram, then used the correlation to obtain the land surface moisture availability, called the temperature–vegetation cover index ($TVCI$), which ranges from 0.0 to 1.0. Considering that f_c represents vegetation density more directly, we replaced the $NDVI$ with f_c. The $TVCI$ multiplies potential evapotranspiration to calculate actual LE. LE_p is partitioned into two components: potential plant transpiration and potential soil evaporation. Finally, a revised sine-curve model was constructed to estimate ET_d by adding an exponent to the Jackson *et al.* (1983) sine function. In addition, high-resolution Thematic Mapper (TM)/Enhanced Thematic Mapper Plus (ETM$^+$) data combined with ground-measured data were used to calculate LE and ET_d using our algorithm for the farmlands of the North China Plain.

2. The methods

Our algorithm is divided into five parts, which calculate the following variables: *TVCI*, aerodynamic resistance (r_a), *VI*, R_n, *G*, *LE* and ET_d (figure 1). The inputs to the model include remote-sensing data and measured land-surface data. The remotely sensed data are T_s, surface albedo (α), and *NDVI*; the measured land-surface data incorporate T_a, actual vapour pressure (e_a), wind speed (u), and surface solar radiation (Q), vegetation height, and leaf area index (*LAI*). In addition, the diurnal pattern of the surface solar radiation is needed. T_a is used here only for calculating effective atmospheric emissivity, the Richardson number, and the slope of the saturated vapour pressure as a function of air temperature, instead of *TVCI*.

2.1 *Temperature–vegetation cover index (*TVCI*)*

In this study, we constructed the f_c–T_s trapezoidal diagram for regional *TVCI* under the following four assumptions:

(1) It is assumed that for a given f_c condition ($f_c > 0$), there always exist several 'dry points' and 'wet points' where surface actual *LE* is close to 0 and to LE_p, respectively.

(2) Under a given f_c condition ($f_c > 0$), *TVCI* increases linearly as T_s increases.

(3) Under a given surface moisture condition, T_s decreases linearly as f_c increases ($f_c > 0$).

(4) The slope of the 'wet edge' is given as 0.

According to these assumptions, the dry edge is a simulated straight line whose slope is less than 0, whereas the wet edge is also a simulated straight line but with a slope
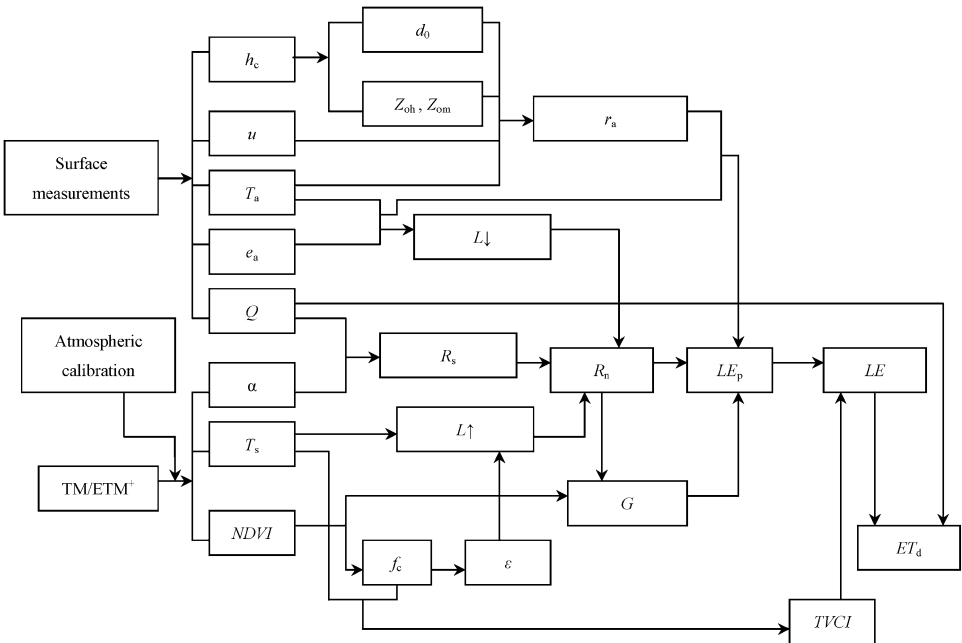
Figure 1.   Flowchart of the improved regional evapotranspiration algorithm based on high-resolution Landsat-TM/ETM$^+$ and meteorological data.

of 0. Almost all of the pixels are included in the VI–T_s trapezoid diagram, and a linear interpolation for any pixel is conducted for an estimation of $TVCI$, which ranges from 0 to 1 (figure 2).

According to the assumptions, $TVCI$ can be estimated as

$$TVCI = \frac{T_{s\min} - T_s}{T_{s\min} - T_{s\max}} \tag{1}$$

where $T_{s\min}$ and $T_{s\max}$ are the minimum and maximum T_s under a given f_c, respectively; T_s is the spectral surface temperature under a given pixel; and $T_{s\max}$ and $T_{s\min}$ are the surface temperatures of the dry edge and wet edge, respectively (figure 2). A nonlinear correlation between $T_{s\max}$ and f_c is assumed (Carlson *et al.* 1995a). Owing to simplification, a linear correlation between them is usually applied (Moran *et al.* 1994, Sandholt *et al.* 2002), which can be expressed as

$$T_{s\max} = a_1 + b_1 f_c \tag{2}$$

where a_1 and b_1 are parameters defining the dry edge. The parameters a_1 and b_1 are estimated based on pixels from a large area that can represent an entire range of surface moisture contents, from wet to dry, and from bare soil to fully vegetated surfaces (Sandholt *et al.* 2002). $T_{s\min}$ is usually regarded as a constant that is difficult to estimate owing to the effects of clouds, sloping terrain, and standing water on T_s. For calculating $T_{s\min}$, the first pixels in a remote-sensing image covered by clouds
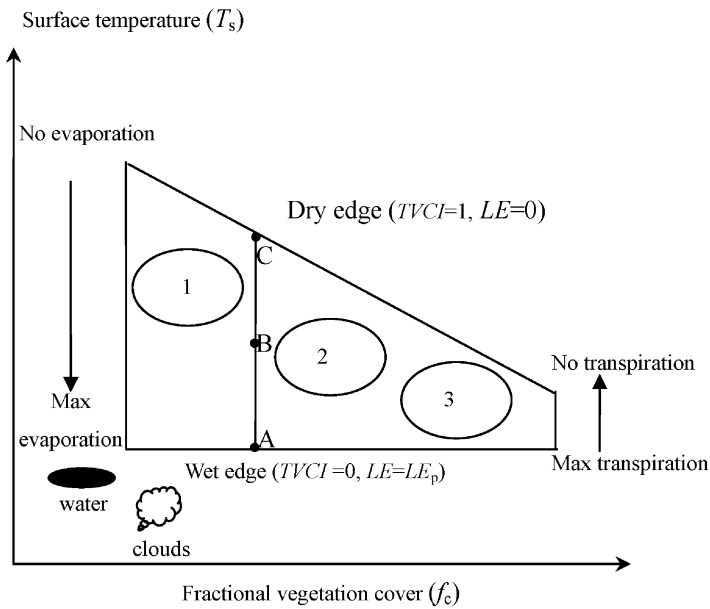
Figure 2. Correlation between fractional vegetation cover (f_c) and surface temperature (T_s in °C). Adapted from Lambin and Ehrlich 1996. f_c, fractional vegetation cover; $TVCI$, temperature–vegetation cover index; LE, latent heat flux; LE_p, potential latent heat flux; $TVCI$ at point B is equal to the ratio of AB to AC. 1: bare soil; 2: partial vegetation cover; 3: full vegetation cover.

are removed because T_s of those pixels is evidently lower than that of other pixels. The effect of sloping terrain is not considered in our research area, the North China Plain, for which slope is negligible. For pixels covered with standing water, f_c is relatively low. A threshold for f_c, 0.5, is chosen in the study. T_{smin} is estimated according to the averaged minimum T_s under the condition that f_c is greater than 0.5. In addition, the averaged minimum T_s at small f_c intervals (0.01) is regarded as T_{smin}.

The *TVCI* isolines are similar to those of Sandholt *et al.* (2002), and their slopes are lower than 0 according to figure 2. The difference between the present study and that by Sandholt *et al.* (2002) is that we used f_c–T_s trapezoid diagrams to estimate *TVCI*, instead of using triangular *NDVI*–T_s diagrams, because f_c can reflect vegetation density more directly than *NDVI*. Moreover, the triangular f_c–T_s diagrams must be replaced with trapezoid diagrams since *ET* should change with surface soil moisture at the maximum f_c condition.

2.2 Net radiation (R_n) and soil heat flux (G)

For calculating LE_p, first the net radiation (R_n) and soil heat flux (G) should be estimated. R_n is calculated as

$$R_n = (1-\alpha)Q + L\downarrow - L\uparrow \tag{3a}$$

$$R_n = (1-\alpha)Q + \varepsilon\sigma\left(\varepsilon_a T_a^4 - T_s^4\right) \tag{3b}$$

where Q is solar short-wave radiation, $L\downarrow$ is down-welling long-wave radiation from the atmosphere, $L\uparrow$ is upward long-wave radiation from the surface, T_s is radiometric surface temperature, T_a is air temperature, α is spectral surface albedo, ε is surface emissivity, σ is the Stefan–Boltzmann constant, and ε_a is effective atmospheric emissivity (Brutsaert 1975). Li and Lyons (1999) calculated ε from the vegetation fraction and the emissivity of bare soil and vegetation as

$$\varepsilon = \varepsilon_v f_c + \varepsilon_s(1-f_c) \tag{4}$$

where ε_v is vegetation emissivity (assumed to be 0.98), ε_s is bare soil emissivity (assumed to be 0.96), and f_c is the fractional vegetation cover. f_c is estimated from *NDVI* by

$$f_c = \left(\frac{NDVI - NDVI_{min}}{NDVI_{max} - NDVI_{min}}\right)^2 \tag{5}$$

where $NDVI_{min}$ is the seasonal minimum vegetation index and $NDVI_{max}$ is the seasonal maximum vegetation index.

Under vegetation-covered conditions, G is determined by R_n, T_s, α, and *NDVI* from the function (Bastiaanssen 1995)

$$G = \Gamma R_n \tag{6}$$

$$\Gamma = \frac{T_s - 273.16}{\alpha}\left(0.0032\alpha + 0.0062\alpha^2\right)\left(1 - 0.978NDVI^4\right) \tag{7}$$

Under bare soil conditions,

$$G = 0.23R_n \qquad (8)$$

2.3 *Aerodynamic resistance (r_a)*

Based on the Monin–Obukhov surface layer, the aerodynamic resistance can be expressed as (Li and Lyons 1999, Zhang *et al.* 1995)

$$r_a = r_{ah} + r_x \qquad (9)$$

$$r_{ah} = \frac{1}{k^2 u}\left[\ln\left(\frac{z_r - d_0}{Z_{om}}\right) - \psi_m\right]\left[\ln\left(\frac{z_r - d_0}{Z_{oh}}\right) - \psi_h\right] \qquad (10)$$

$$r_x = kB^{-1}\frac{1}{k^2 u}\left[\ln\left(\frac{z_r - d_0}{Z_{om}}\right) - \psi_m\right] \qquad (11)$$

where r_{ah} is the resistance to heat transfer; r_x is the extra resistance; d_0 is the zero displacement height; Z_{om} is the roughness length for momentum; Z_{oh} is the roughness length for heat; k is von Karman's constant (0.4); u is the wind speed at the reference height z_r; and ψ_h, and ψ_m are stability correction functions for heat and momentum, respectively.

Z_{om} and d_o are estimated from crop height (h_c) as

$$d_0 = 0.67h_c \qquad (12)$$

$$Z_{om} = 0.13h_c \qquad (13)$$

h_c for crops are estimated from the *LAI*. Polynomial equations relating h_c and *LAI* are constructed based on the results of our field measurements

$$h_c = 0.0115LAI^3 - 0.0887LAI^2 + 0.2782LAI \quad R^2 = 0.99 \quad \text{(for wheat)} \quad (14)$$

$$h_c = 0.0623LAI^3 - 0.4825LAI^2 + 1.432LAI \quad R^2 = 0.97 \quad \text{(for maize)} \quad (15)$$

The two polynomial equations for calculating h_c are only suitable before the flowering stage of wheat (DOY 120) and maize (DOY 220). After flowering, crop *LAI* declines, while crop h_c reaches a maximum and remains constant thereafter. Thus, h_c maps for wheat and maize at the flowering stage are applied to the research area after flowering. For calculating *LAI* on a regional scale, an exponential correlation between *LAI* and *NDVI* is found according to our experiments (figure 3). The empirical correlation is suitable under the condition that *NDVI* is greater than 0.05. When *NDVI* is less than 0.05, land surface is regarded as a non-vegetation condition, where h_c is given as a constant (0.01 m). In the research area, vegetation is classified as crops and woodland. h_c of woodland is assumed as a constant (10 m) according to our observation.

Carlson *et al.* (1995c) noted that the parameter KB^{-1} takes into account a combination of effects: the difference between aerodynamic and radiometric temperatures, the vertical distribution of thermal radiation within the vegetation, the angular effect of radiometric temperature, energy exchanges between different surfaces, etc. The aerodynamic KB^{-1} is identical to $\ln(Z_{om}/Z_{oh})$. In addition, Z_{oh} is
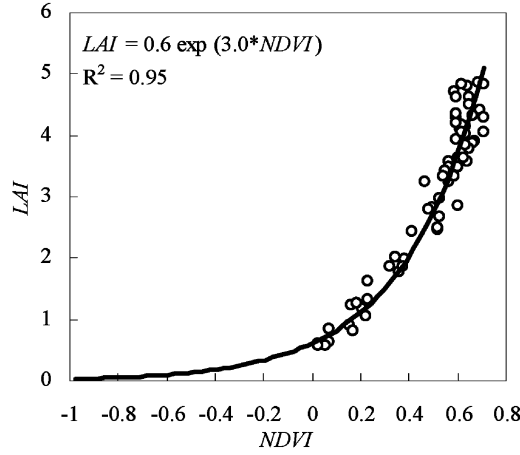
Figure 3. The exponential correlation between the normalized difference vegetation index (*NDVI*) and leaf area index (*LAI*).

estimated as

$$Z_{oh} = Z_{om} \exp\left(-6.27 k u^{*\frac{1}{3}}\right) \tag{16}$$

$$u^* = \frac{ku}{\ln((z_r - d_0)/Z_{om})} \tag{17}$$

where u^* is the friction wind speed.

The stability correction functions can be determined using the Businger–Dyer formulations (Businger 1988, Sugita and Brutsaert 1990) for unstable conditions, which yield the following expressions:

$$\psi_m = 2\ln\left(\frac{1+x}{2}\right) + \ln\left(\frac{1+x^2}{2}\right) - 2acr\tan(x) + \frac{\pi}{2} \tag{18}$$

$$\psi_h = 2\ln\left(\frac{1+x^2}{2}\right) \tag{19}$$

For stable conditions (Webb 1970)

$$\psi_m = \psi_h = -5\xi \tag{20}$$

where $x = (1-16\zeta)^{1/4}$ and $\zeta = (z_r - d)/L_o$, in which L_o is the Obukhov stability length.

The stability factor ζ can be replaced by the Richardson number (R_i) using the following relationships (Thom 1975, Businger 1988)

$$R_i = \begin{cases} \xi & \text{Unstable} & (21a) \\ \dfrac{\xi}{1+5\xi} & \text{stable} & (21b) \end{cases}$$

with

$$R_i = \frac{5g(z_r - d_0)(T_s - T_a)}{u^2((T_a + T_s)/2 + 273.16)} \tag{22}$$

where g is the acceleration due to gravity ($=9.8\,\mathrm{m\,s^{-2}}$).

2.4 *Vegetation index* (NDVI)

NDVI is calculated from the reflectance in the red and near-infrared bands as

$$NDVI = \frac{\alpha_{nir} - \alpha_{red}}{\alpha_{nir} + \alpha_{red}} \tag{23}$$

where α_{nir} and α_{red} are the reflectivity of the near-infrared and red bands, respectively. The near-infrared and red bands for Landsat-TM/ETM+ are bands 4 and 3, respectively.

2.5 *Latent heat flux* (LE) *and daily evapotranspiration* (ET$_d$)

Moran *et al.* (1994) assumed a linear correlation between *TVCI* and instantaneous latent heat flux (LE_i), which is calculated as

$$LE_i = (1 - TVCI)LE_p \tag{24}$$

with

$$LE_p = f_c LE_{pv} + (1 - f_c)LE_{ps} \tag{25}$$

where LE_{pv} and LE_{ps} are the potential vegetation transpiration and potential soil evaporation, respectively. LE_{pv} and LE_{ps} are estimated as

$$LE_{pv} = \frac{\Delta R_{nc} + \rho_a C_p VPD/r_a}{\Delta + \gamma(1 + r_{cp}/r_a)} \tag{26}$$

$$LE_{ps} = \frac{\Delta}{\Delta + \gamma}(a' \, R_{ns} + b' \, R_{ns}^2/R_n) \tag{27}$$

where Δ is the slope of the saturated vapour pressure as a function of air temperature, L is the latent heat of vaporization for water, γ is the psychrometric constant, ρ_a is the air density, R_{ns} is the soil net radiation, R_{nv} is the vegetation net radiation, *VPD* is the atmospheric vapour pressure deficit, r_a is the aerodynamic resistance, r_{cp} is the canopy resistance at potential evapotranspiration as estimated from r_{sp}/LAI (r_{sp} is the minimum stomatal resistance), and a' and b' are coefficients. These coefficients are given as 0.92 and 0.4, respectively (Rey 1999). R_{ns} and R_{nv} are calculated as

$$R_{ns} = R_n \exp(-k'LAI) \tag{28}$$

$$R_{nc} = R_n - R_{ns} \tag{29}$$

where *LAI* is the leaf area index, and k' is the attenuation coefficient of R_n, which is given as 0.55.

Jackson *et al.* (1983) assumed that the instantaneous solar radiation (Q_i) that strikes the Earth on a clear day closely conforms to the relation

$$Q_i = Q_m \sin(\pi t/N) \tag{30}$$

where Q_m is the maximum irradiance at solar noon, t is the time (beginning at sunrise), and N is the time period (hours) between sunrise and sunset. At solar noon,

$t=N/2$ and $Q_i=Q_mN$ can be calculated using the sunset hour angle, ω_0, which is evaluated according to geographic latitude (ψ), and solar declination (δ)

$$\omega_0 = \cos^{-1}(-tg\psi tg\delta) \tag{31}$$

The day length $N=(2\omega_0)$ is expressed in hours as follows

$$N = \frac{2}{15}\cos^{-1}(-tg\psi tg\delta) \tag{32}$$

Owing to its simplicity, Jackson's sine method is widely used to simulate Q_i from Q_m (Zhang and Lemeur 1995, Boegh *et al.* 1999). However, the method gives convex curves because Q_i is overestimated in the early morning and in the late afternoon (Wang *et al.* 2002). In order to provide non-convex curves, we introduced a new parameter (b). Thus, Q_i is a function of Q_m in our revised sine function

$$Q_i = Q_m \sin^b(\pi t/N) \tag{33}$$

where the parameter b is an exponent of the sine function, reflecting impacts of geographic latitude, solar declination, and degree of cloudiness on the convexity of the diurnal patterns of solar radiation. A nonlinear iterative method can be used to determine the value of b from the solar time and its corresponding solar radiation. This revised sine function simulates Q_i quite well compared with the Jackson sine function (figure 4).

According to the revised function, daily solar radiation can be calculated by means of the following integral:

$$Q_d = \int_0^N Q_m \sin^b(\pi t/N)\, dt \tag{34}$$

Based on the assumption that $Q_i/Q_m=LE_i/LE_m$, instantaneous LE_i can be estimated as

$$LE_i = LE_m \sin^b(\pi t/N) \tag{35}$$

where LE_m is the maximum LE at solar noon.
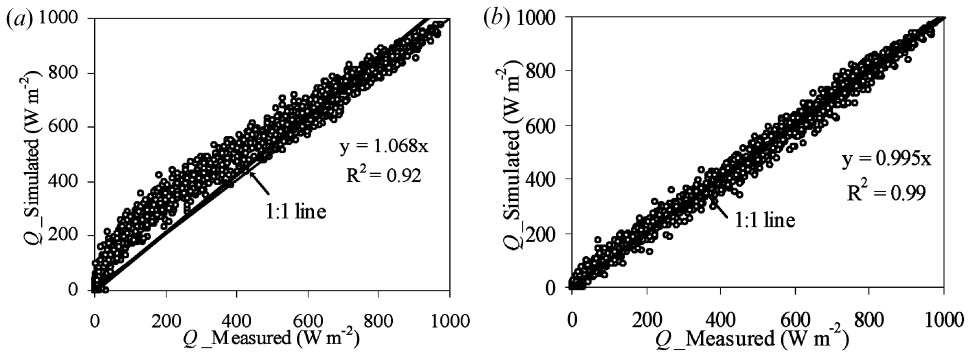
Figure 4.   Comparison of the measured total solar radiation (Q_Measured (W m^{-2})) and simulated solar radiation (Q_simulated (W m^{-2})) with the (*a*) original sine function and (*b*) the revised sine function.

ET_d can be estimated by means of the LE integral between sunrise and sunset:

$$ET_d = \frac{1}{L} \int_0^N LE_m \sin^b(\pi t/N)\, dt \qquad (36)$$

$$ET_d = \frac{1}{L} \frac{\int_0^N \sin^b(\pi t/N)\, dt}{\sin^b(\pi t_i/N)} LE_i \qquad (37)$$

where t_i is the satellite's overpass time.

By substituting LE_i with $TVCI$ and LE_p, we obtain

$$ET_d = \frac{1}{L} \frac{\int_0^N \sin^b(\pi t/N)\, dt}{\sin^b(\pi t_i/N)} LE_i = \frac{(1 - TCVI)E_p}{\sin^b(\pi t_i/N)} \int_0^N \sin^b(\pi t/N)\, dt \qquad (38)$$

where E_p is the potential evaporation rate at the satellite's overpass time.

In the same way as the measured LE is obtained with the Bowen Ration Energy Balance (BREB) system, LE estimated with the trapezoid diagram is integrated with the sine method or the revised sine method to provide an estimate of ET_d. By comparing ET_d measurements made by the BREB system, it can be seen that the revised sine method estimated ET_d better than the original sine method (figure 5). For the revised sine method, there was no systematic deviation from the 1 : 1 line, but the previous method overestimated ET_d due to its overestimation of Q (figure 4).

3. Area description and data preparation

3.1 *Area description*

The research area is located in the North China Plain (NCP), a region with a history of more than 2000 years of cultivation. The research area is a high-yield farming plain with fertile topsoil and high organic content in a loam soil (Zhang *et al.* 2002).
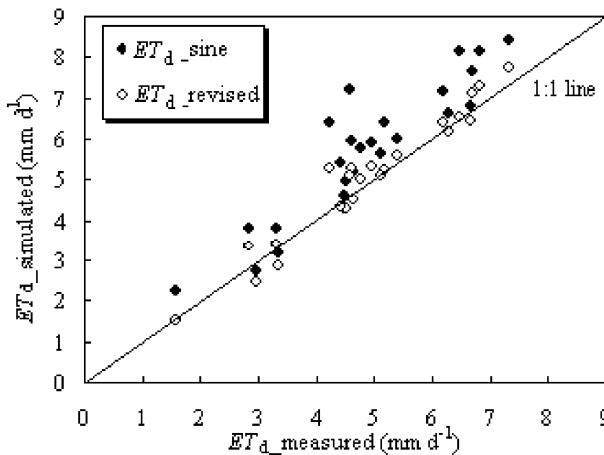
Figure 5. Comparison of the measured daily evapotranspiration (ET_d (mm d^{-1})) with the Bowen Ratio Energy Balance (BREB) system and the simulated values (mm d^{-1}) with the sine method and the revised sine method. ET_d_sine: ET_d estimated using the sine method; ET_d_revised: ET_d estimated using the revised sine method.

With a temperate semi-arid monsoon climate, the area has a mean annual temperature of 12.2°C. The mean annual global radiation is $524\,\mathrm{kJ\,cm^{-2}}$ and the mean annual precipitation is 481 mm, most of which occurs from late June to September. Rotation cropping of winter wheat and maize is one of the most extensive planting systems in the Plain. The growing season for winter wheat is from early October to mid-June, and summer maize is planted at the end of the winter wheat season and is harvested in late September. Rainfall does not meet the needs of wheat for normal growth, especially during the dry and windy spring season. Therefore, five to six periods of irrigation are needed to maintain high grain yield. During the summer, rainfall is usually enough for the water consumption needs of maize, but two to three irrigations are needed in a dry year.

3.2   *Preparing remote-sensing data*

Landsat TM/ETM$^+$ data were used over an area of $33.3\,\mathrm{km} \times 34.8\,\mathrm{km}$ with path/row: 124/34. Only TM/ETM$^+$ data that were little affected by clouds were chosen for the study. In total, there were 12 TM/ETM$^+$ datasets in 2000–2002 selected for the study.

Processing of the TM/ETM$^+$ data was carried out as follows. The original TM/ETM$^+$ digital number (DN) data were georeferenced. First, the DN image in each visible and near-infrared band was saved as a *.raw format image. The raw images were atmospherically calibrated with 6s radiative transfer codes. The atmospherically calibrated images were then input into the ENVI 3.6 image processing software to acquire the reflectance of narrow bands and the surface vegetation index, *NDVI*. Surface albedo (α) was obtained from the reflectance of narrow bands, namely bands 1, 3, 4, 5, and 7 (Liang *et al.* 2003).

The thermal band of the TM/ETM-6 was used to deduce T_s. An empirical form of Planck's function (http://ltpwww.gsfc.nasa.gov/IAS/handbook/handbook_site_map.html.) was used to estimate the temperature at the top of the atmosphere with sensor radiances. Since there are no radiosonde data available near the research area to calibrate to surface values, we used standard mid-latitude summer radiosonde data, the mean terrain altitude, and an estimate of atmospheric visibility as the inputs to an atmosphere radiative transfer model, MODTRAN (version 4.0) (Kneizys *et al.* 1996, Arthur-Hartranft *et al.* 2003).

3.3   *Land-surface observations*

Land-surface experiments were conducted at the Luancheng Agro-ecosystem Station (LAES) (37° 53′ N, 114° 41′ E, 50.1 m a.s.l.), one of 34 agricultural ecosystem stations of the Chinese Ecological Research Network. Air temperature, absolute humidity, total solar radiation, wind speed at the reference height, and crop height were measured at the Landsat TM/ETM overpass time (LST 10:50). The vegetation index, surface albedo, surface temperature, and surface soil moisture were measured during the wheat and maize seasons of 2001. Vegetation at different growth stages was captured weekly with a digital colour camera (Model-4, Dycam, Inc., Chatsworth, CA, USA). Additional vegetation measurements with the camera were conducted at the satellite's overpass time. The captured pictures were processed using the DYCAMB software provided by Dycam, Inc. to acquire the vegetation index, *NDVI*. Total solar radiation and reflected solar radiation were measured with two pyranometers (type CM3, Kipp & Zonen, Inc., Delft, The Netherlands).

Integrated surface temperature was measured with an infrared radiometer (type ER-2008, Minolta, Inc., Mahwah, NJ), which was mounted on a remote-sensing tower at a height of 28 m pointing 45° towards the surface for the stationary recording of integrated surface temperature. The pyranometer and the infrared radiometer were connected with a datalogger (type CR21X, Campbell, Inc., Logan, UT) that automatically collected data every 20 minutes. Owing to a fault in the datalogger, some data were lost. These lost data were not gap-filled and were thus not used in the study. Crop leaf areas and crop heights were measured by hand from 10 randomly selected plants harvested from the sampling area while the crop pictures were being captured. *LAI* was determined according to the measured crop leaf areas and crop density. Gravimetric soil water content at 0–10 cm depth was measured by taking 3.5-cm soil cores with a hollow steel drill at three sites at the satellite's overpass time. This was changed into volumetric soil water content according to the soil density (Zhang *et al.* 2002).

Crop ET_d was measured by a large-scale weighing lysimeter, which weighs about 2 tonne empty and about 14 tonne when full of soil, with a water depth measurement precision of 0.02 mm (Liu *et al.* 2002, Zhang *et al.* 2002). The crop in the lysimeter was the same as the surrounding crop: wheat or maize. The conditions of irrigation and fertilization in the lysimeter were basically the same as those in the farmland. The BREB system has been operating at the station since March 1999. It stopped in August 2003. Due to the flat terrain and the wind fetch length of more than 250 m, the system estimated *LE* well compared with the lysimeter (Zhang *et al.* 2002). Thus, in the study, surface *LE* estimated with the BREB system was used to calibrate the value provided by the *VI-T*$_s$ trapezoid method.

4. Results and analysis

4.1 *Analysis of inputs*

T_s, *NDVI*, and α, estimated from the atmospherically calibrated Landsat TM/ETM$^+$ DN numbers, were compared with land-surface observations at the station (figure 6(*a*)–(*c*)). Remotely estimated α closely paralleled with the land-surface observed T_s (figure 6(*a*)), and remotely-sensed T_s and *NDVI* also were consistent with the observed values at the station (figures 6(*b*) and (*c*)). Owing to the failure of the datalogger, not all surface-observed data were collected at the overpass time of the Landsat 5/7. The comparison between the observed data and the calibrated remotely sensed data suggests that it is reasonable to use T_s, *NDVI*, and α estimated from Landsat TM/ETM$^+$ data as the inputs of our algorithm.

4.2 *Analysis of outputs*

Estimates of instantaneous *LE* using our algorithm were compared with measurements from the BREB system (figure 7). There was a good agreement between the measured *LE* and the estimated values, with a small root-mean-squared error (RMSE) of 50.1 W m^{-2}. No significant deviation from the diagonal 1 : 1 line was found between the calculated and measured *LE* within the range of 100 to 600 W m^{-2}. Therefore, the algorithm can be reliably used for the estimation of instantaneous *LE*. The ET_d values estimated with our revised sine function were compared with the lysimeter-measured values (figure 8). The RMSE of 0.93 mm d^{-1} indicated that there was an acceptable agreement between the measured and
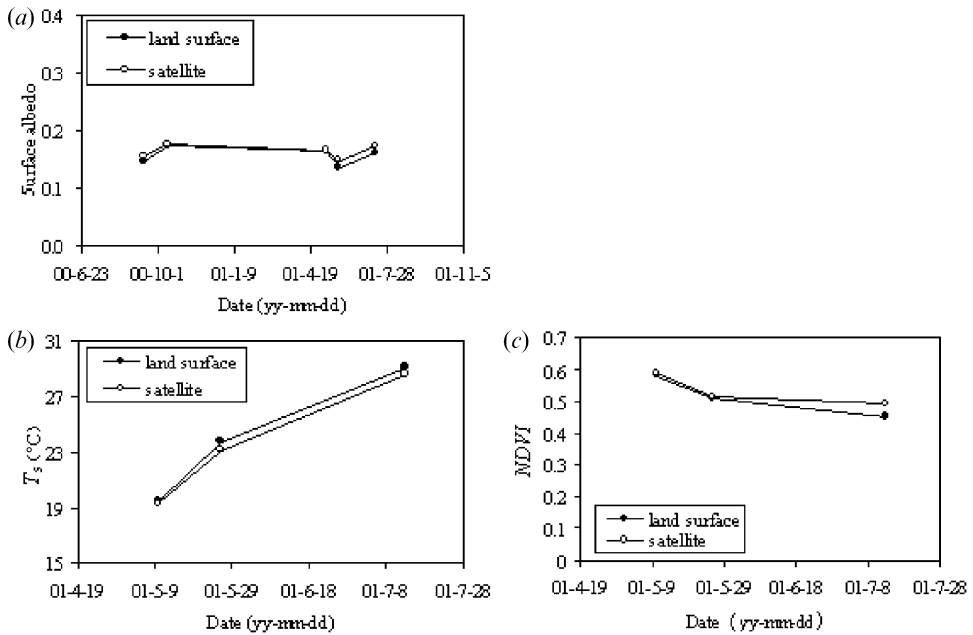
Figure 6. Comparison of measurements at the Luancheng Agro-ecosystem station, Chinese Academy of Sciences (CAS), of (*a*) surface albedo, (*b*) surface temperature, and (*c*) Normalized Difference Vegetation Index (*NDVI*) with values obtained from the Landsat-TM/ ETM[+] sensors.

estimated ET_d. Also, there was no significant deviation from the diagonal 1:1 line between estimated and measured ET_d.

Some errors may have been inadvertently introduced into the above algorithm. First, spatial-scale effects must be considered. The BREB system measured *LE* with a wind-fetch length of 200 m in the upwind direction, whereas the large-scale
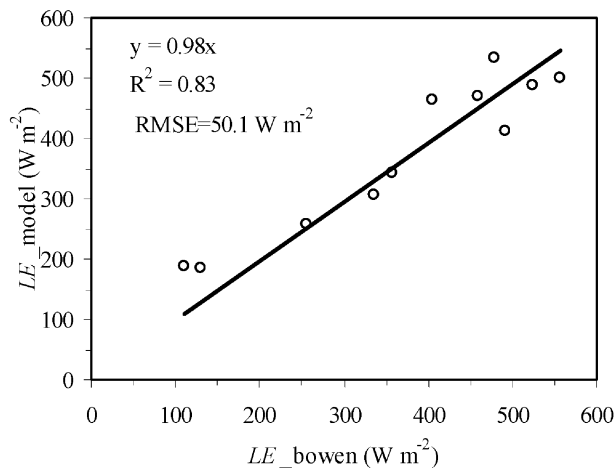
Figure 7. Comparison of latent heat flux from measurements (*LE*_bowen (W m^{-2})) with the Bowen Ratio Energy Balance (BREB) system and from the simulation (*LE*_model (W m^{-2})) with the regional evapotranspiration algorithm. RMSE: root mean square error.
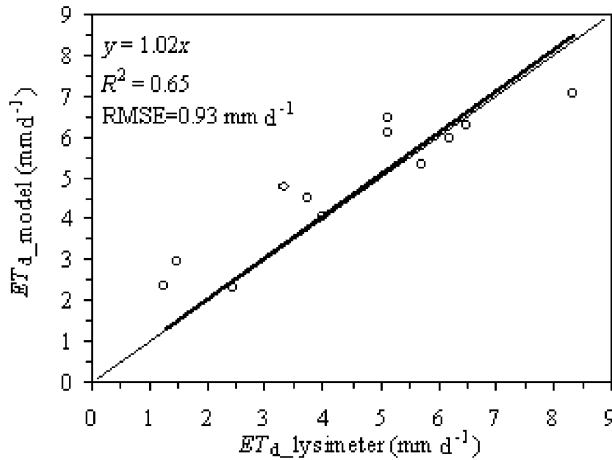
Figure 8. Comparison of daily evapotranspiration between the measurement (ET_{d}_lysimeter (mm d^{-1})) with the large-scale weighing lysimeter and the simulation (ET_{d}_model (mm d^{-1})) with the regional evapotranspiration algorithm. RMSE: root mean square error.

weighing lysimeter measured ET_{d} only within an area of $2 \times 1.5\,\mathrm{m}^2$. Moreover, the algorithm based on the TM/ETM$^+$ data covered an area as large as $30\,\mathrm{m} \times 30\,\mathrm{m}$. The difference in the area of interest among the different approaches could cause some errors if the focused parameters (variables) change with area. Second, the mismatch in times may also cause disagreements between the estimates and the measurements. The lysimeter measurements at 8:00 and 20:00, and the measured ET_{d} were obtained from the weight difference between the two times; however, the algorithm estimates ET_{d} from the integral of LE from sunrise to sunset. Moreover, the BREB system cannot measure the dew point temperature accurately in some cases. Under advective conditions, the theoretical basis for BREB is not correct, and this influences the measured precision of LE.

4.3 *Parameter analysis*

The *TVCI* of each pixel was interpolated in the trapezoid from the dry edge to the wet edge (figure 2). In order to determine the slope and intercept that defined the dry edge, the maximum T_{s} observed for small intervals of f_{c}, was extracted in the $T_{\mathrm{s}}/f_{\mathrm{c}}$ space (figure 9), and the slope and intercept of the dry edge were then acquired using least-squares linear regression (table 1). Only values of f_{c} greater than 0.1 were used to fit the dry edge, since the maximum T_{s} increased with increasing f_{c} at small f_{c} at that time. Maximum T_{s} at small f_{c} is mainly controlled by solar radiation, instead of by the surface soil moisture condition. The slopes of the dry edges appeared as if they corresponded well with the phenological development of the crops, e.g. the changes in the leaf area index (*LAI*) (table 1). After wheat revived in March 2001, the slope of the dry edge increased with increasing *LAI* from 31 March 2001, to 10 May 2001. The slope decreased with the decrease of *LAI* from 10 May 2001 to 19 June 2001, when the crop was harvested. Similar results were reported by Goetz (1997), who reported that the slope of $T_{\mathrm{s}}/NDVI$ was determined largely by the vegetation and environmental conditions (e.g. leaf area index and soil moisture), and
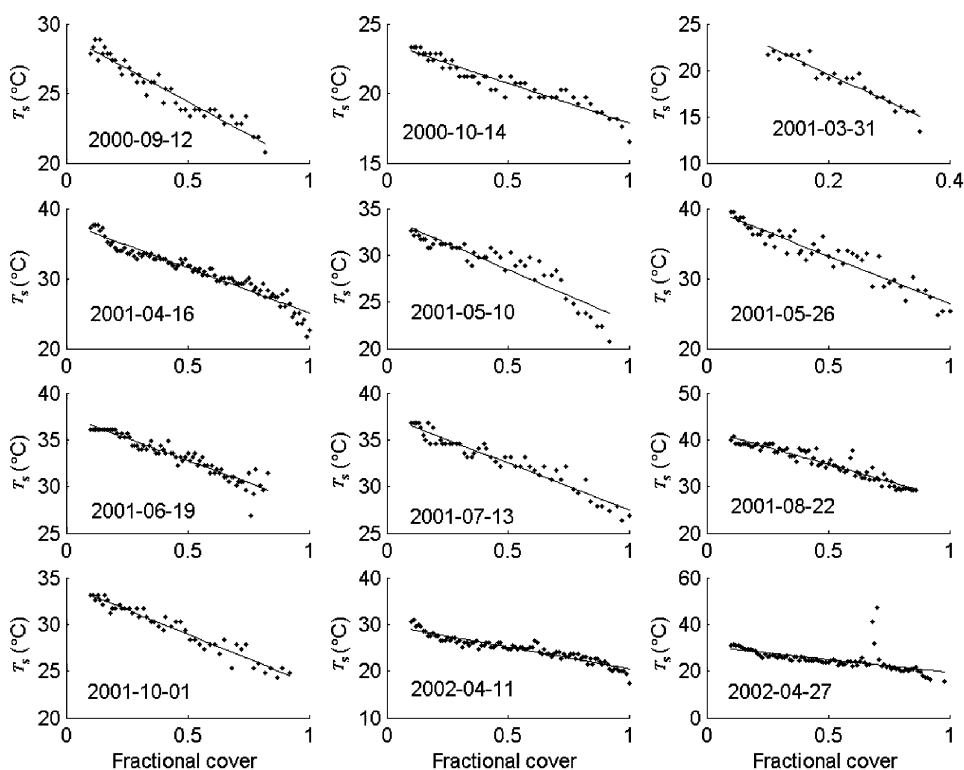
Figure 9. Dry edges used for estimation of the temperature vegetation cover index (*TVCI*). Maximum surface temperature (T_{smax}) was extracted from small intervals (0.01) of fractional vegetation cover, and the dry edge was fitted by linear regression equations.

Table 1. Leaf area index (*LAI*) measured at the Luancheng Station and the output parameters of the regional evapotranspiration algorithm based on the vegetation index (*VI*)-surface temperature (T_s) trapezoid correlation.

Date (yy-mm-dd)	Crop	LAI^*	Slope of dry edge	Intercept of dry edge (°C)	T_s of wet edge (°C)	Exponent of the revised sine model
00-09-12	maize	3.0	−11.83	29.81	20.03	1.46
00-10-14	wheat (sowed)	0.0	−7.94	24.60	14.62	0.91
01-03-31	wheat	3.0	−16.24	25.43	13.19	1.44
01-04-16	wheat	4.0	−13.65	35.57	19.67	1.37
01-05-10	wheat	4.8	−12.35	34.10	17.80	1.77
01-05-26	wheat	3.0	−12.84	39.31	21.74	1.47
01-06-19	wheat (harvested)	0.2	−13.10	37.31	26.82	1.66
01-07-13	maize	1.5	−10.09	36.97	24.35	1.91
01-08-22	maize	4.5	−14.51	39.76	29.20	1.53
01-10-01	maize (harvested)	0.0	−10.85	33.85	20.82	1.57
02-04-11	wheat	3.5	−11.15	28.96	15.39	2.01
02-04-27	wheat	4.3	−13.79	29.59	11.59	1.69

*LAI was measured in the field at the Luancheng Station, Chinese Academy of Science.
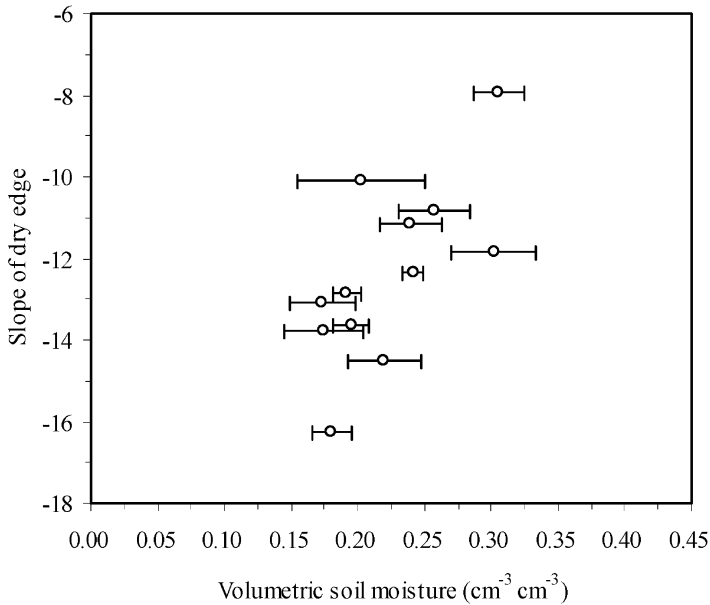
Figure 10. Correlation between volumetric soil moisture and the slope of the dry edge. Pearson correlation analysis shows that the correlation is significant at the 0.01 level (two-tailed).

was thus related to the partition of energy fluxes. An evident correlation between the slope of T_s/f_c and the 0–10 cm soil moisture was found (figure 10), which supports the hypothesis that, except for f_c, soil moisture is an important secondary control on radiometric surface temperature due to its effect on soil thermal inertia (Friedl and Davis 1994).

The wet edge temperature, T_{smin}, was fitted according to the relationship between the minimum temperature for the f_c intervals and its corresponding f_c. T_{smin} was estimated as the mean minimum temperature for the f_c intervals (Sandholt *et al.* 2002). There was no significant correlation between T_{smin} and crop phenology, since T_{smin} is affected not only by crop phenology, but also by other factors, including clouds, sloping terrain, and standing water. In order to reduce the effect of standing water on T_s, we chose T_s under the condition f_c over 0.5, whereas, interference also exists from the impact of standing water on T_s. The influence of fractional clouds on T_s is usually not easy to eliminate. This may explain the low dependence of T_{smin} on crop *LAI* in the current study.

The exponent b of our revised sine function for ET_d was generally greater than 1.0 except for the data on 14 October 2000. The maximum was as large as 2.01 on 11 April 2002 (table 1). On most selected days, ET_d with the Jackson sine function was overestimated compared with the value calculated using our revised sine function (equations (35) and (39)). Over a fixed daylight period ($N=12$ hours), simulated ET_d decreases as the parameter b increases, and the rate of declension of the simulated ET_d with respect to parameter b increases as LE_m increases (figure 11). Following the analysis, we were able to conclude that the errors in ET_d with the Jackson sine method will increase continuously as the actual
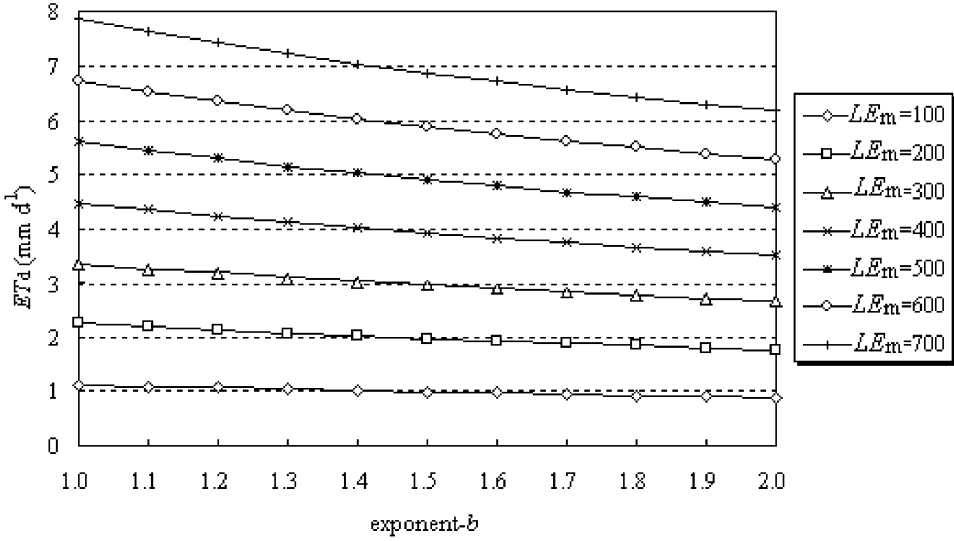
Figure 11. Theoretical analysis of the correlation between the exponent b and simulated daily evapotranspiration (ET_d (mm d^{-1})) under different maximum latent heat flux (LE_m (W m^{-2})) scenarios (daylight period is assumed to be $N=12.0$ h).

LE_m and the actual exponent b increase. The errors also seem higher on clear days than on cloudy days.

4.4 *Sensitivity analysis*

There were six variables and parameters, namely, r_{sp}, h_c, VPD, f_c, Q and u, chosen for a sensitivity analysis of the algorithm (figure 12(*a*)–(*f*)). With an increase in r_{sp}, LE decreased linearly with a slope of -1.18 (figure 12(*a*)). Minimum canopy resistance, r_{cp}, was estimated from r$_{sp}$/LAI. A proposed range for crop r_{sp} is from 25.0 to 100.0 s m^{-1} (Moran *et al.* 1994). r_{sp} for broadleaved herbaceous crops is about 80.0 s m^{-1} (Kelliher *et al.* 1995). Under well-irrigated conditions, r_{sp} for winter wheat at this station was about 50 s m^{-1} (Zhang and Jiang 2001). Thus, r_{sp} in this study was given a constant value of 50 s m^{-1}. Variation of r_{sp} from 25 to 100 s m^{-1} caused a maximum error of 59.0 W m^{-2} on 26 May 2001. Figure 12(*b*) shows the impact of h_c variation on LE. Crop h_c influences aerodynamic variables, e.g. Z_{om} and d_o. For a 0.1-m increase or decrease in h_c, LE changed by 12.9 W m^{-2} (figure 12(*b*)). It produces small errors because h_c for wheat and maize was well estimated from LAI using equations (15) and (16). Atmospheric VPD affects the degree of stomatal opening, and influences water loss from plants to the atmosphere. With an increase of 0.1 kPa in VPD, LE increased by 12.0 W m^{-2} (figure 12(*c*)). Thus, VPD seems a sensitive factor for LE. In addition, LE increases more gradually at high than at low VPD values. In this study, LE changed little when VPD was greater than 1.5 kPa. The change of f_c has impacts on T_{smax} (equation (2)) and ε (equation (5)). Sensitivity analysis of f_c shows that LE decreases with an increase in f_c. LE declined by only about 49.1 W m^{-2} when f_c increased from 0 to 1 (figure 11(*d*)). LE increases linearly with Q and u. For a measured error in Q of 100.0 W m^{-2}, the error for LE was 46.0 W m^{-2}, and for a 1.0 m s^{-1} measured error in u, the error for LE was 23.7 W m^{-2} (figures 12(*e*) and (*f*)).
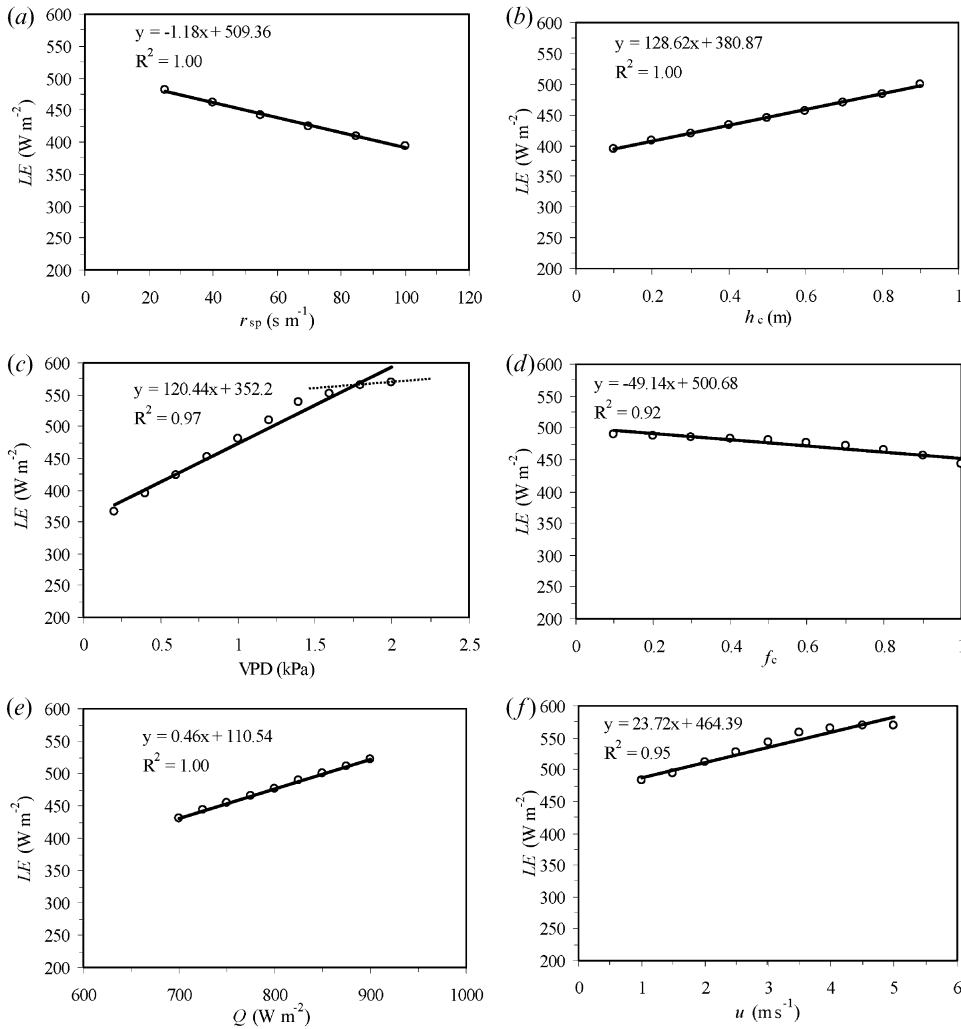
Figure 12. Sensitivity analysis for six variables and parameters in the regional evapotranspiration algorithm (26 May 2001). r_{sp}, minimum stomatal resistance (s m^{-1}); h_c, crop height (m); VPD, vapour pressure deficit (kPa); f_c, fractional vegetation index; Q, solar radiation (W m^{-2}); u, wind speed (m s^{-1}).

5. Concluding remarks

A regional ET algorithm was constructed to calculate the surface $TVCI$ from a trapezoidal VI–T_s space, and to determine LE_p from LE_{pv} and LE_{ps}. A revised sine function was used to estimate ET_d from simultaneous LE at the satellite's overpass time. The models using the trapezoidal VI–T_s space to estimate $TVCI$ were shown to be more flexible, simple, and versatile than previous models that require more parameters. Validations of the algorithm using ground-measured data confirmed that the model performs well for the North China Plain.

It is necessary to use the parameter b to simulate the diurnal variation of Q and LE since by its use, the degree of convexity of the diurnal pattern of Q and LE can be accounted for in the early morning and the late afternoon. The parameter is

jointly determined by latitude, solar declination, and degree of cloudiness. Differences in latitude can cause the parameter b to vary at different geographic locations, and solar declination can cause seasonal variations at a site. Weather conditions can vary greatly from clear to cloudy. Our preliminary research showed that during days with a short period of cloud cover, the exponent b did not vary significantly compared with cloud-free days; however, the exponent noticeably increased on days when clouds prevailed for a long time. Usually, solar radiation data at meteorological sites can be obtained easily. Thus, we can map the exponent b from different meteorological sites in order to accurately estimate ET_d on a regional scale.

A sensitivity analysis of LE as a function of six variables and parameters elucidated how LE could be affected by changes in these factors. The parameter r_{sp} was set to $50\,\mathrm{s\,m^{-1}}$ to obtain a result with relatively small errors (figure 12(a)). However, the value of r_{sp} should be carefully determined using ground-based measurements if the model is to be applied to different crops or regions. f_c deduced from $NDVI$ had little influence on LE (figure 12(d)). The surface variables, h_c, VPD, Q and u, showed a certain impact on LE (figure 12(b),(c),(e),(f)), especially for VPD. VPD is usually measured with some errors because the wet bulb temperature cannot be measured accurately. In the study, we have not mapped Q, VPD and u by interpolation between different meteorological sites because the research area, with an area of $33.3\,\mathrm{km} \times 34.8\,\mathrm{km}$, is not particularly big and there is no other suitable meteorological station near the research area. For improving the accuracy of the algorithm on a large regional scale, it is necessary to carefully map the surface variables at the satellite's overpass time.

For a wider application of the trapezoidal diagram method, some attention should be paid to the following considerations. First, when using the trapezoidal diagram to estimate $TVCI$, we must be careful to consider the impact of clouds, standing water, and sloping terrain on T_s. As mentioned in the description of the study area the North China Plain is very flat. For areas with more complex terrain, a Digital Elevation Model (DEM) should be used to calibrate satellite-estimated T_s and the effect of clouds and standing water should also be eliminated. For a large research area with different climatic or vegetational conditions, it is recommended that the surface variables be measured at multiple points. Second, LE and ET_d should be measured to calibrate the outputs of the algorithm at these points. Changes in $TVCI$ within the trapezoidal VI–T_s space may become a potential research topic. For simplicity, we considered only linear changes in $TVCI$ from the dry edge to the wet edge in our study. We understand that $TVCI$ may change nonlinearly, and the nature of this change must be clarified in the future.

References

ARTHUR–HARTRANFT, S.T., CARLSON, T.N. and CLARKE, K.C., 2003, Satellite and ground-based microclimate and hydrologic analyses coupled with a regional urban growth model. *Remote Sensing of Environment*, **86**, pp. 385–400.

BASTIAANSSEN, W.G.M., 1995, Regionalization of surface flux densities and moisture indictors in composite terrain. PhD thesis, Wageningen Agricultural University, Wageningen, The Netherlands.

BOEGH, E., SOEGAARD, H., HANAN, N., KABAT, P. and LESCH, L., 1999, A remote sensing study of the NDVT–T_s relationship and the transpiration from sparse vegetation in the Sahel based on high-resolution satellite data. *Remote Sensing of Environment*, **69**, pp. 224–240.

BRUTSAERT, W.H., 1975, On a derivable formula for long-wave radiation from clear skies. *Water Resources Research*, **11**, pp. 742–744.

BUSINGER, J.A., 1988, A note on the Businger–Dyer profiles. *Boundary-Layer Meteorology*, **42**, pp. 145–151.

CARLSON, T.N., GILLIES, R.R. and SCHMUGGE, T.J., 1995a, An interpretation of methodologies for indirect measurement of soil–water content. *Agricultural and Forest Meteorology*, **77**, pp. 191–205.

CARLSON, T.N., CAPEHART, W.J. and GILLIES, R.R., 1995b, A new look at the simplified method for remote–sensing of daily evapotranspiration. *Remote Sensing of Environment*, **54**, pp. 161–167.

CARLSON, T.N., TACONET, O., VIDAL, A., GILLES, R.R., OLIOSO, A. and HUMES, K., 1995c, An overview of the Workshop on Thermal Remote-Sensing held at La-Londe-Les-Maures, France, 20–24 September, 1993. *Agricultural and Forest Meteorology*, **77**, pp. 141–151.

CHURKINA, G., RUNNING, S.W. and SCHLOSS, A.L., 1999, Comparing global models of terrestrial net primary productivity (NPP): the importance of water availability. *Global Change Biology*, **5**, pp. 46–55.

CRACKNELL, A.P. and XUE, Y., 1996, Estimation of ground heat flux using AVHRR data and an advanced thermal inertial model (SoA–TI model). *International Journal of Remote Sensing*, **17**, pp. 637–642.

DUNKEL, Z. and SZENYÁN, I.G., 2000, Estimation of areal distribution of evapotranspiration using remotely sensed data during vegetation period in Hungary. *Advances in Space Research*, **26**, pp. 1051–1054.

FRIEDL, M.A. and DAVIS, F.W., 1994, Sources of variation in radiometric surface-temperature over a tallgrass prairie. *Remote Sensing of Environment*, **48**, pp. 1–17.

GILLIES, R.R., CARLSON, T.N., CUI, J., KUSTAS, W.P. and HUMES, K.S., 1997, A verification of the 'triangle' method for obtaining surface soil water content and energy fluxes from remote measurements of the Normalized Difference Vegetation Index (NDVI) and surface radiant temperature. *International Journal of Remote Sensing*, **18**, pp. 3145–3166.

GOETZ, S.J., 1997, Multi-sensor analysis of NDVI, surface temperature and biophysical variables at a mixed grassland site. *International Journal of Remote Sensing*, **18**, pp. 71–94.

IBANEZ, M. and CASTELLVI, F., 2000, Simplifying daily evapotranspiration estimates over short full-canopy crops. *Agronomy Journal*, **92**, pp. 628–632.

JACKSON, S.H., 1991, Relationships between normalized leaf water potential and crop water-stress index values for acala cotton. *Agricultural Water Management*, **20**, pp. 109–118.

JACKSON, R.D., REGINATO, R.J. and IDSO, S.B., 1977, Wheat canopy temperature: a practical tool for evaluating water requirements. *Water Resources Research*, **13**, pp. 651–656.

JACKSON, R.D., HATFIELD, J.L., REGINATO, R.J., IDSO, S.B. and PINTER, P.J., 1983, Estimation of daily evapotranspiration from one time-of-day measurements. *Agricultural Water Management*, **7**, pp. 351–362.

Jiang, L. and Islam, S., 2001, Estimation of surface evaporation map over southern Great Plains using remote sensing data. *Water Resources Research*, **37**, pp. 329–340.

Jiang, L. and Islam, S., 2003, An intercomparison of regional latent heat flux estimation using remote sensing data. *International Journal of Remote Sensing*, **24**, pp. 2221–2236.

Kelliher, F.M., Leuning, R., Raupach, M.R. and Schulze, E.D., 1995, Maximum conductances for evaporation from global vegetation types. *Agricultural and Forest Meteorology*, **73**, pp. 1–16.

Kneizys, F.X., Abreu, L.W., Anderson, G.P., Chetwynd, J.H., Shettle, E.P., Berk, A., Bernstein, L.S., Robertson, D.C., Acharya, P., Rothman, L.S., Selby, J.E.A., Gallery, W.O. and Clough, S.A., 1996, The MODTRAN 2/3 report and LOWTRAN 7 model, Ontar, Massachusetts.

Kustas, W.P. and Norman, J.M., 1996, Use of remote sensing for evapotranspiration monitoring over land surfaces. *Hydrological Sciences Journal*, **41**, pp. 495–516.

Lagouarde, J.P., 1991, Use of NOAA AVHRR data combined with an agrometeorological model for evaporation mapping. *International Journal of Remote Sensing*, **12**, pp. 1853–1864.

Lambin, E.F. and Ehrlich, D., 1996, The surface temperature–vegetation index space for land cover and land-cover change analysis. *International Journal of Remote Sensing*, **17**, pp. 463–487.

Li, F.Q. and Lyons, T.J., 1999, Estimation of regional evapotranspiration through remote sensing. *Journal of Applied Meteorology*, **38**, pp. 1644–1654.

Liang, S.L., Shuey, C.J., Russ, A.L., Fang, H.L., Chen, M.Z., Walthall, C.L., Daughtry, C.S.T. and Hunt, R., 2003, Narrowband to broadband conversions of land surface albedo: II. Validation. *Remote Sensing of Environment*, **84**, pp. 25–41.

Liu, C.M., Zhang, X.Y. and Zhang, Y.Q., 2002, Determination of daily evaporation and evapotranspiration of winter wheat and maize by large-scale weighing lysimeter and micro-lysimeter. *Agricultural and Forest Meteorology*, **111**, pp. 109–120.

Moran, M.S., Clarke, T.R., Inoue, Y. and Vidal, A., 1994, Estimating crop water-deficit using the relation between surface-air temperature and spectral vegetation index. *Remote Sensing of Environment*, **49**, pp. 246–263.

Moran, M.S., Rahman, A.F., Washburne, J.C., Goodrich, D.C., Weltz, M.A. and Kustas, W.P., 1996, Combining the Penman–Monteith equation with measurements of surface temperature and reflectance to estimate evaporation rates of semiarid grassland. *Agricultural and Forest Meteorology*, **80**, pp. 87–109.

Nemani, R.R. and Running, S.W., 1989, Estimation of regional surface-resistance to evapotranspiration from NDVI and thermal–IR AVHRR data. *Journal of Applied Meteorology*, **28**, pp. 276–284.

Nemani, R., Pierce, L., Running, S. and Goward, S., 1993, Developing satellite-derived estimates of surface moisture status. *Journal of Applied Meteorology*, **32**, pp. 548–557.

Nichols, W.E. and Cuenca, R.H., 1993, Evaluation of the evaporative fraction for parameterization of the surface, energy-balance. *Water Resources Research*, **29**, pp. 3681–3690.

Nishida, K., Nemani, R.R., Running, S.W. and Glassy, J.M., 2003, An operational remote sensing algorithm of land surface evaporation. *Journal of Geophysical Research*, **108**, p. 4270, doi: 10.1029/2002JD002062.

Rey, J.M., 1999, Modelling potential evapotranspiration of potential vegetation. *Ecological Modelling*, **123**, pp. 141–159.

Sandholt, I. and Andersen, H.S., 1993, Derivation of actual evapotranspiration in the Senegalese Sahel, using NOAA-AVHRR data during the 1987 growing season. *Remote Sensing of Environment*, **46**, pp. 164–172.

SANDHOLT, I., RASMUSSEN, K. and ANDERSEN, J., 2002, A simple interpretation of the surface temperature/vegetation index space for assessment of surface moisture status. *Remote Sensing of Environment*, **79**, pp. 213–224.

STEWART, J.B., KUSTAS, W.P., HUMES, K.S., NICHOLS, W.D., MORAN, M.S. and DEBRUIN, H.A.R., 1994, Sensible heat-flux radiometric surface-temperature relationship for 8 semiarid areas. *Journal of Applied Meteorology*, **33**, pp. 1110–1117.

SUGITA, M. and BRUTSAERT, W., 1990, Regional surface fluxes from remotely sensed skin temperature and lower boundary-layer measurements. *Water Resources Research*, **26**, pp. 2937–2944.

THOM, A.S., 1975, Momentum, mass and heat exchange of plant communities. In *Vegetation and the Atmosphere*, J.L. Monteith (Ed.), pp. 57–109 (London: Academic Press).

WANG, S., CHEN, W.J. and CIHLAR, J., 2002, New calculation methods of diurnal distribution of solar radiation and its interception by canopy over complex terrain. *Ecological Modelling*, **155**, pp. 191–204.

WEBB, E.K., 1970, Profile relationships: The log-linear range, and extension to strong stability. *Quarterly Journal of the Royal Meteorological Society*, **112**, pp. 857–889.

XUE, Y., LAWRENCE, S.P., LLEWELLYN-JONES, D.T. and MUTLOW, C.T., 1998, On the Earth's surface energy exchange determination from ERS satellite ATSR data. Part 1: long-wave radiation. *International Journal of Remote Sensing*, **19**, pp. 2561–2583.

XUE, Y., LLEWELLYN-JONES, D.T., LAWRENCE, S.P. and MUTLOW, C.T., 2000, On the Earth's surface energy exchange determination from ERS satellite ATSR data: Part 2: Short-wave radiation. *International Journal of Remote Sensing*, **21**, pp. 3415–3426.

ZHANG, L. and LEMEUR, R., 1995, Evaluation of daily evapotranspiration estimates from instantaneous measurements. *Agricultural and Forest Meteorology*, **74**, pp. 139–154.

ZHANG, L., LEMEUR, R. and GOUTORBE, J.P., 1995, A one-layer resistance model for estimating regional evapotranspiration using remote-sensing data. *Agricultural and Forest Meteorology*, **77**, pp. 241–261.

ZHANG, Y.Q. and JIANG, J., 2001, Effects of soil-water stress condition on water transfer process of winter wheat leaves. *Arid Zone Research*, **18**, pp. 57–61 (in Chinese).

ZHANG, Y.Q., LIU, C.M., SHEN, Y.J., KONDOH, A., TANG, C.Y., TANAKA, T. and SHIMADA, J., 2002, Measurement of evapotranspiration in a winter wheat field. *Hydrological Processes*, **16**, pp. 2805–2817.

Appendix. Nomenclature

α	surface albedo
γ	psychrometric constant
δ	solar declination
Δ	the slope of the saturated vapour pressure as a function of air temperature ($kPa\,{}^{\circ}C^{-1}$)
ε	surface emissivity
ε_a	effective atmospheric emissivity
ε_s	bare soil emissivity
ε_v	vegetation emissivity
ζ	stability factor
ρ_a	air density ($g\,m^{-3}$)
σ	Stefan–Boltzman constant ($W\,m^{-2}\,K^{-4}$)
ψ	geographic latitude
ψ_h	stability correction function for heat
ψ_m	stability correction function for momentum
ω	hour angle (south zero, west positive)

ω_0 sunset hour angle

d_0 displacement height (m)

d_{om} roughness length for momentum (m)

DOY   day of year

ET_d daily evapotranspiration (mm d^{-1})

E_p potential evapotranspiration (mm d^{-1})

f_c fractional vegetation cover

g acceleration due to gravity (m s^{-2})

G soil heat flux (W m^{-2})

H sensible heat flux (W m^{-2})

h_c crop height (m)

k von Karman's constant

L latent heat of vaporization for water (J g^{-1})

L$\uparrow$ upwards long-wave radiation from the surface (W m^{-2})

L$\downarrow$ down-welling long-wave radiation from the atmosphere (W m^{-2})

LAI leaf area index

LE latent heat flux (W m^{-2})

LE_i instantaneous latent heat flux (W m^{-2})

LE_m maximum latent heat flux at solar noon (W m^{-2})

LE_p potential latent heat flux (W m^{-2})

LE_{ps} potential soil evaporation (W m^{-2})

LE_{pv} potential vegetation transpiration (W m^{-2})

L_o Obukhov stability length (m)

N daylight period (hours)

$NDVI$ normalized difference vegetation index

Q solar radiation (W m^{-2})

Q_d total daily irradiance (MJ m^{-2} d^{-1})

Q_i instantaneous solar radiation (W m^{-2})

Q_m maximum solar radiation at solar noon (W m^{-2})

r_a aerodynamic resistance (s m^{-1})

r_{ah} resistance to heat transfer (s m^{-1})

r_{cp} canopy resistance at potential evapotranspiration (s m^{-1})

R_i Richardson number

R_n net radiation (W m^{-2})

R_{ns} soil net radiation (W m^{-2})

R_{nv} vegetation net radiation (W m^{-2})

r_x extra resistance (s m^{-1})

t_i overpass time of satellite

T_a air temperature (°C)

T_s radiometric surface temperature (°C)

T_{smax} maximum surface temperature (°C)

T_{smin} minimum surface temperature (°C)

$TVCI$ temperature vegetation cover index

u wind speed (m s^{-1})

u^* friction wind speed (m s^{-1})

VPD vapour pressure deficit (kPa)

Z_{oh} roughness length for heat (m)

z_r reference height (m)